Supporting information for "Topology-empowered membrane devices for terahertz photonics"

Quanlong Yang[a,b,*], Dongyang Wang[c], Sergey Kruk[a], Mingkai Liu[a], Ivan Kravchenko[d], Jiaguang Han[e], Yuri Kivshar[a], and Ilya Shadrivov[a,*]

[a]Nonlinear Physics Centre, Research School of Physics, Australian National University, Canberra ACT 2601, Australia
[b]School of Physics and Electronics, Central South University, Changsha 410083, Hunan, China
[c] Department of Physics, The Hong Kong University of Science and Technology, Clear Water Bay, Hong Kong 999077, China
[d]Center for Nanophase Materials Sciences, Oak Ridge National Laboratory, TN 37831, USA
[e]Center for Terahertz Waves and College of Precision Instrument and Optoelectronics Engineering, Tianjin University, Tianjin, 300072, China

1. Valley-Chern number of VHPCs

VHPCs feature non-zero Berry curvatures localized at K and K' valleys, and the Berry curvatures can be calculated either numerically or based on the plane wave expansion method with the analytically derived Hamiltonian. Moreover, the Berry curvature has the same magnitude but opposite in sign for K and K' valleys, the total Berry curvature of a single band is zero, but integrated Berry curvature around a valley is nearly (not exactly) quantized, and it defines the valley-Chern invariant in the Valley Hall system. The Chern number assigned to the n-th band is defined by

$$\begin{aligned} C_n &= \frac{1}{2\pi i}\int d^2\, k F_{12}(k), \\ F_{12}(k) &= \partial_1 A_2(k) - \partial_2 A_1(k), \\ A_u(k) &= \langle n(k)|\partial_u|n(k)\rangle. \end{aligned} \tag{1}$$

Where $A_u(k)$ is the Berry connection (u=1, 2), and $|n(k)\rangle$ is the normalized wave function of the Bloch band obtained from the Hamiltonian equation.

We here show the numerical example of calculation of the valley-Chern number based on the proposed unit cell. The electric field distributions in a unit cell can be numerically calculated for the eigenmode, from which we retrieved the periodic part of the Bloch function as |n(k)>. We then numerically calculate

the Berry curvature for the 1st band (within 1.25×1.25 size of the Brillouin zone) as shown below in Fig. S1. We can see that the nontrivial Berry curvature of opposite sign appears around the two valleys.

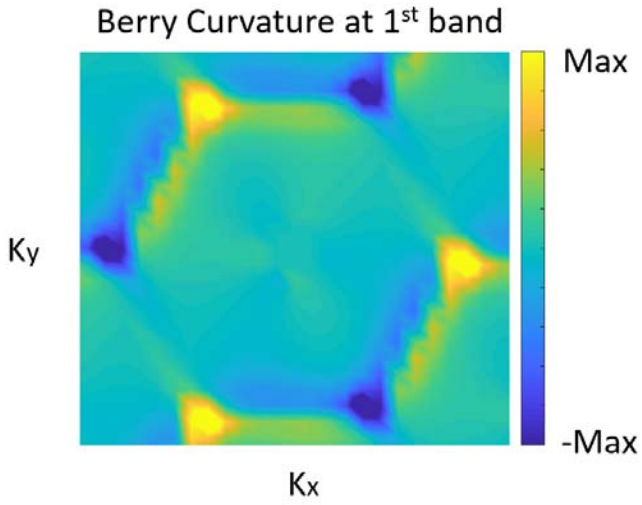

Figure S1. The numerically calculated Berry curvature for the 1st band based on the proposed unit cell in 2D. a region of 1.25×1.25 Brillouin zone is shown. The integral of Berry curvature averaged for a valley is around F12 ≈ 1.1π for a valley (30×30 numerical data points), which is closed to be half (π) quantized.

2. Experiment details of topological devices

We fabricate the metasurface on a silicon-on-insulator wafer with a high-resistivity 90-μm-thick silicon layer, 1-μm-thick buried oxide layer and a 300-μm-thick handle wafer. Both polished sides of the wafer are initially coated with 1-μm-thick silicon oxide. Standard photolithography is employed to delineate the pattern of the membrane metasurface in the photoresist film. After a hard bake, this photoresist layer is used to conduct a plasma etching process of the silicon oxide film which, in turn, served as the hard mask during deep reactive etching of the device layer. After the resist removal and surface cleaning, the resulting metasurface in the device layer is passivated by plasma-enhanced chemical vapor deposition of a 1.4 μm-thick silicon oxide to provide the device membrane with protection and mechanical support.

Similar production steps are repeated to etch the windows in the handle layer after a back-side alignment procedure. As a result, there is a rectangular window in the handle wafer at the back of topological devices, which look as membranes suspended on the remaining ribs of the handle wafer. Both the buried oxide layer and the residuals of silicon oxide masks are left on the surfaces when the device fabrication is completed. Due to the small thickness and low refractive index of the silicon oxide layer, it does not influence the performance of topological devices.

In the experiment, a broadband fiber-based terahertz near-field spectroscopy system is employed to characterize the performance of the topological membrane devices. Two terahertz probes are used as the transmitter and detector, respectively. The emitter that serves as a dipole source is mounted on a three-dimension motorized translation stage which enabled 2D scans at a fixed distance from the sample surface. Both in-plane and normal to the plane polarizations are excited from the probe emitter, only the in-plane polarization couples substantially to the topological modes. For the 2D scanning and transmission measurement, the detector probe is placed at either ~50 μm (for scans) or ~30 μm (for single point measurement) above the sample, respectively. Closer placement of the probe to the sample for single point measurements provided greater signal-to-noise ratio, while we had to resort to larger spacing for the scans in order to avoid crashing the probe into the sample due to non-ideally parallel planes of the sample and the scanning area. The 1D and 2D electric field were detected with 20 μm per step in both x and y directions. With the advantages of the time-domain measurement of the near-field setup, both the amplitude and phase of the edge modes at the desired frequencies can be obtained. In the case of WGM ring resonators, due to the limited frequency resolution and signal to noise ratio of our current near-field time-domain spectroscopy, here we are not able to detect these resonances with Q-factors up to several hundreds.

3. Evanescent decay length of the topological edge modes

The edge modes are confined to the straight waveguide and penetrate into each topological crystal by approximately five unit cells (850 μm). Here, we retrieved the decay length of the edge modes according to $E \propto A_0 e^{-y/L}$, and the calculated decay length L in simulations and in experiment are 810 and 780 μm, respectively. The electric field along Line 2 of Fig 2e is oscillating on the scale of the unit cell due to the Bloch function structure of the solution in the periodic structure. The amplitude of this Bloch function is nearly constant, as can be seen from the inset in Fig. 1b. However, due to imperfect coupling between the dipole source and the edge mode, there are propagating modes excited in free-space, and they are also detected by the receiving probe. The free-space propagating modes induce the amplitude decay along the line 2.

4. In-plane field profile of topological four-port coupler.

To show the good agreement of simulated and measured results, we also present 1D electric field profiles along the four-port coupler (lines 1 and 2 in Fig. 3h) and plot them in Fig. S2. The measured field profile of Ey component is also in a good agreement with the calculated results in Figs. 2g, h, which demonstrate the interface confinement and exponential decay of the edge states.

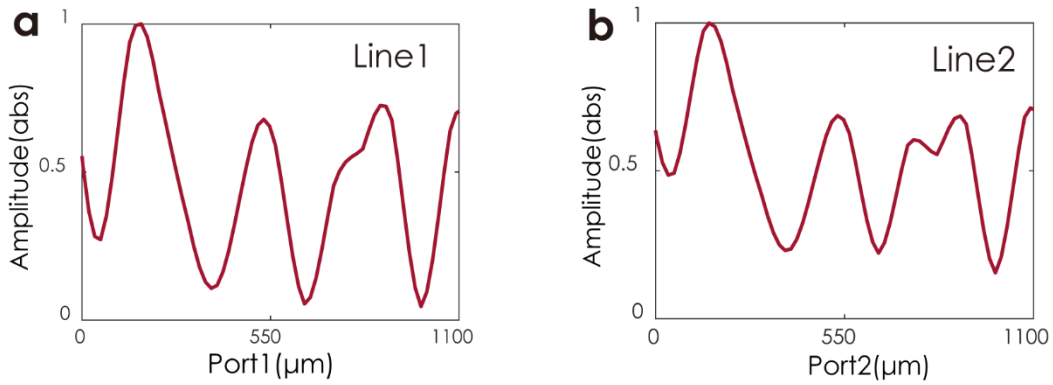

Figure S2| 1D In-plane electric field profile for topological four-port coupler. (a, b) Measured 1D E_y field distributions along the red line 1 and 2 (shown in Fig. 2h of the main manuscript), respectively.

5. In-plane field distribution of topological directional coupler.

Figure S3 illustrates the topological directional coupler with the source placed at different ports. When the source is located in port 1, the edge state σ+ propagates forward along the waveguide 1. Due to the mismatch of the pseudospin, edge state σ+ is not allowed to couple into port 3. After the junction point, part of the edge state σ+ is coupled into port 4, and the rest is coupled into port 2. We find that the electric field profile of the topological directional coupler resembles the microwave one. Based on the same analysis, the other three situations are shown in Figs. 2b-d: source in port 4, σ- → ports 1 and 3; source in port 2, σ- → ports 1 and 3; source in port 3, σ+→ ports 2 and 4. When the edge mode σ+ is excited from Port 1, the normalized transmission spectrum for ports 2 and port 4 is shown Fig. S3e and their transmission ratio is not fixed. For example, the transmission of port 2 and port 4 at 0.5 THz are 56% and 35%, respectively.

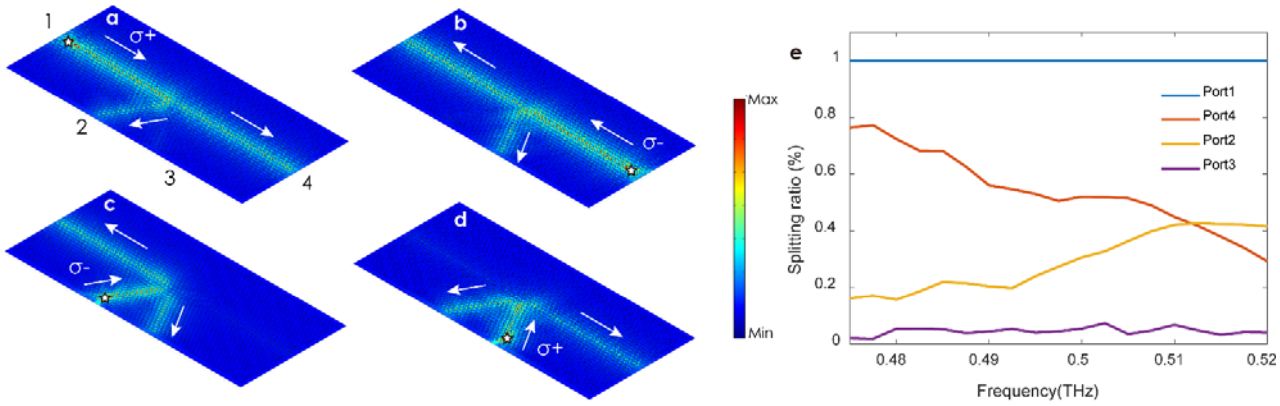

Figure S3| In-plane electric field profile for topological directional coupler. (a) In-plane electric field profile for topological directional coupler with source placed in port 1. The arrows denote the power flow of the edge state. White stars and numbers denotes the excitation source and ports. (b, c, d) Corresponding electric field profiles for the directional coupler with source placed in ports 4, 2 and 3, respectively. (e) Splitting ratio of the powers in different arms of the topological directional coupler with source placed in port 1.

6. Field distribution of topological six-port coupler.

In comparison with the directional coupler, a six-port coupler that consists of six identical DW1 as a combination of the directional coupler and its mirror image. Hence, based on the analysis of the directional coupler, there are four ports that support the valley-locked edge state. From Figure S4, when the topological six-port coupler is excited from port 1, the edge state σ+ propagates forward along port1. After the junction point, the edge state σ+ is coupled into ports 2, 4 and 6, and ports 3 and 5 are prohibited, which matches well with the theoretical prediction. Similarly, when the source is located in port 2, only ports 1, 3 and 5 receive the energy of the edge state σ- from port 2.

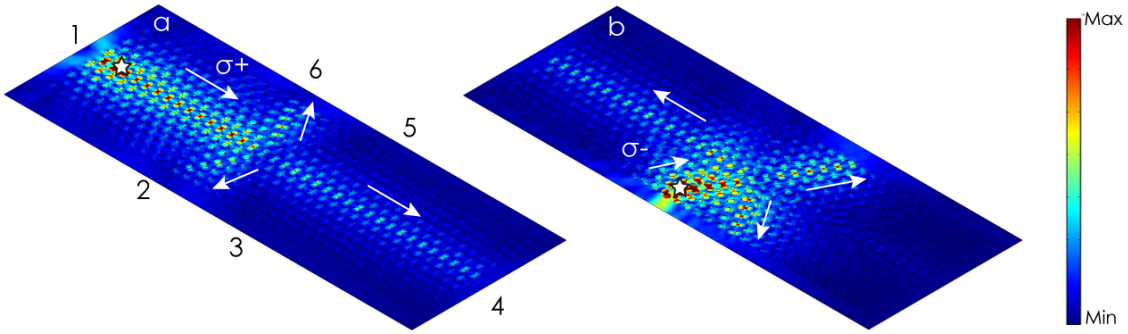

Figure S4| In-plane electric field profile of topological six-port coupler. (a) Electric field profile of topological six-port coupler with source on port 1. (b) Corresponding electric field profile of six-port coupler with source on port 2. The arrows denote the power flow of the edge state. White pentagonal and number denotes the excitation source and ports.

7. Demonstration of topological wave splitter and Mach-Zehnder interferometer.

To demonstrate the performance of the topological wave splitter with the source located in the other ports, Fig. S5a and 4b illustrate the simulated electric field profiles of splitter excited from ports 4 and 2, respectively. When the sources are located in ports 1 and 4, owing to the horizontal symmetry of meta-devices, the field profile of the junction point is also symmetric, which leads to the 50:50 energy division in the topological splitter. However, when the splitter is excited from ports 2 and 3, because of

the asymmetry field profile of the junction points, the edge state that is coupled into ports 1 and 4 displays an uneven wave splitting.

The demonstration of the topological Mach-Zehnder interferometer can be seen in Fig. S5c. Here, the topological interferometer is made by the upper and lower arms as well as the two waveguide ports. When the interferometer is excited from the left port, the edge state is split into two arms with the ratio of 50:50 after the first junction point and join at the second junction point. Due to the same optical path of the two arms, there is a constructive interference at the right port. If we induce a phase shift in one of the arms, e.g. by placing a test sample in one of the arms, the optical path difference in the two arms will modify the interference. Hence, this topological interferometer can be also made on the topological waveguide platform.

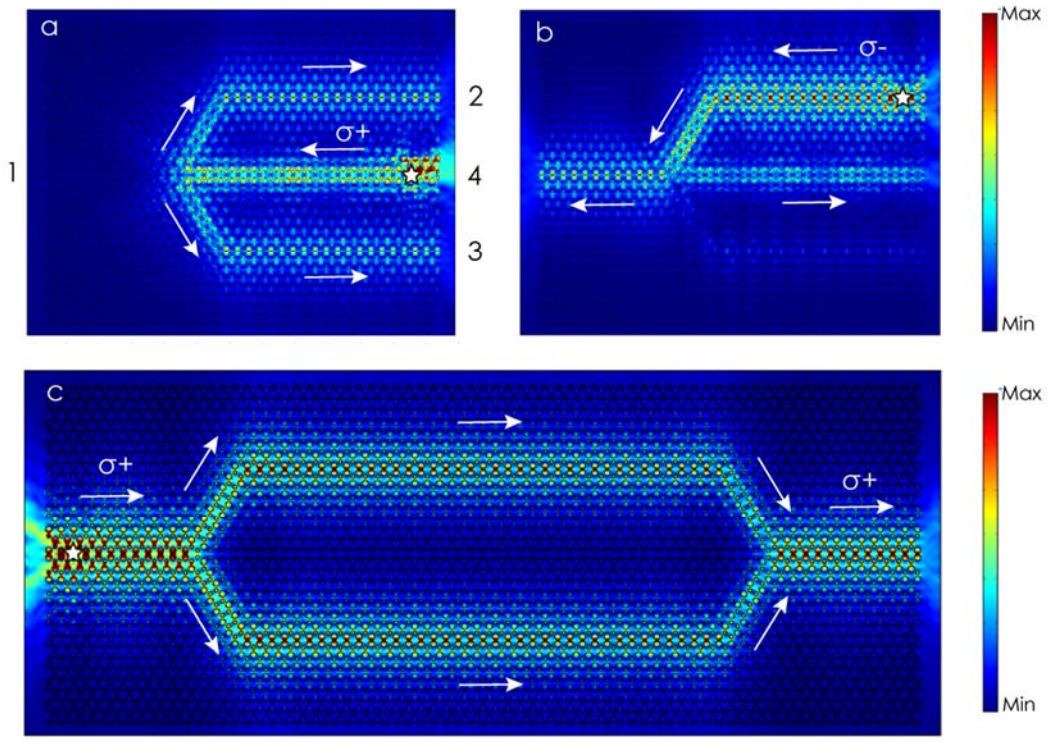

Figure S5| In-plane electric field profile of topological wave splitter and interferometer. (a, b) Electric field profile of topological wave splitter with source on ports 4 and 2, respectively. (c) Corresponding electric field profile of topological

interferometer. Here, the source is located on the left port. The arrows denote the power flow of the edge state. White pentagonal and number denotes the excitation source and ports.

8. SEM images of topological devices demonstrating the quality of the fabrication.

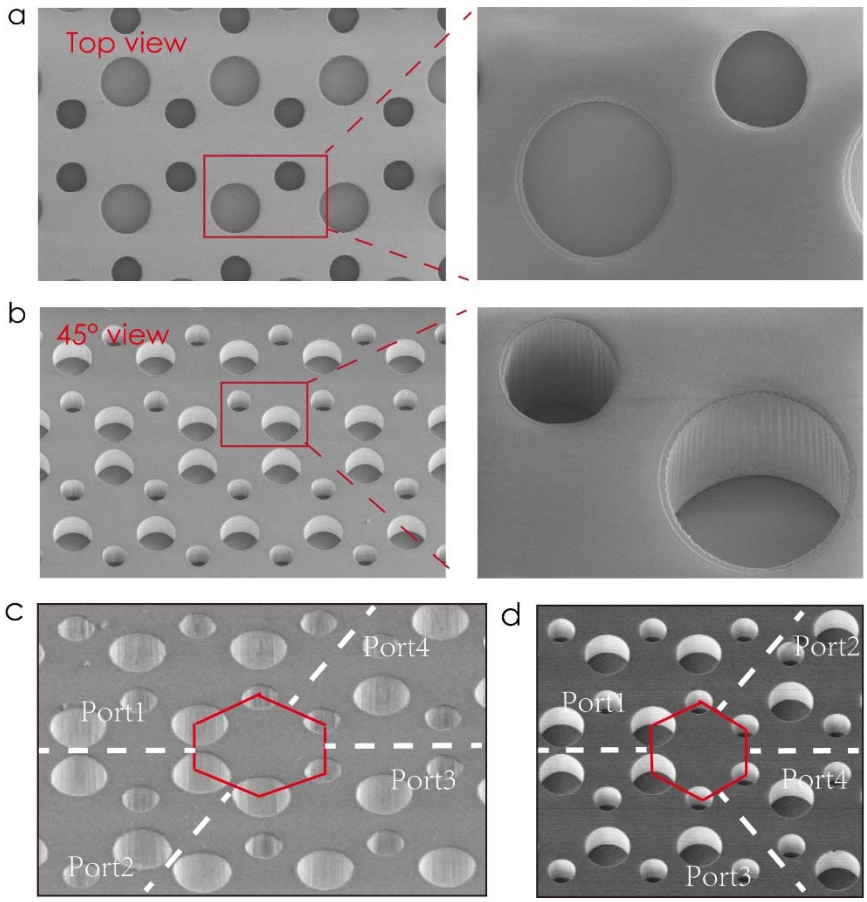

Figure S6| SEM image of topological devices. (a, b) SEM image of VHPC sample in top (a) and 45° view (b). (c, d) SEM image of the junction point from multi-port coupler (c) and splitter (d).

9. Schematic of topological whispering ring resonator.

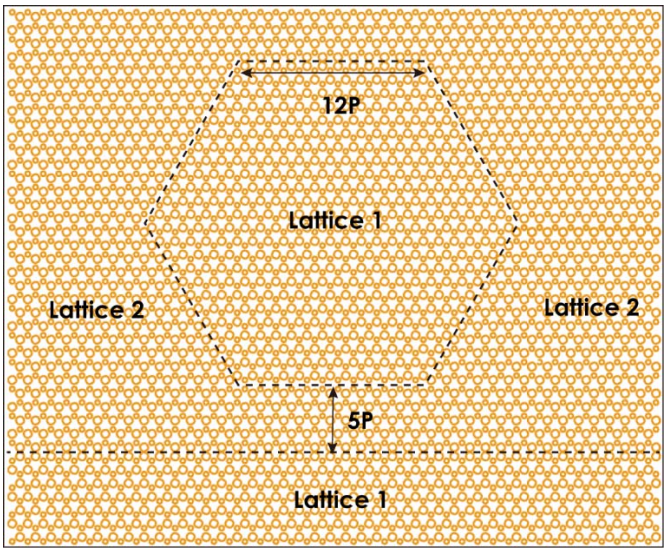

Figure S7| Schematic of topological whispering ring resonator.